Computers and Electronics in Agriculture 196 (2022) 106863

Contents lists available at ScienceDirect

Computers and Electronics in Agriculture

journal homepage: www.elsevier.com/locate/compag

Exploring the potential of hyperspectral imaging to detect Esca disease complex in asymptomatic grapevine leaves

Claudia Pérez-Roncal [a], Silvia Arazuri [a], Carlos Lopez-Molina [b], Carmen Jarén [a], Luis G. Santesteban [c], Ainara López-Maestresalas [a,*]

[a] Department of Engineering, ETSIAB-ISFOOD, Universidad Pública de Navarra, Campus de Arrosadia 31006, Pamplona, Spain
[b] Department of Statistics, Computer Science and Mathematics, ETSIAB, Universidad Pública de Navarra, Campus de Arrosadia 31006, Pamplona, Spain
[c] Department of Agricultural Engineering, Biotechnology and Food, ETSIAB, Universidad Pública de Navarra, Campus de Arrosadia 31006, Pamplona, Spain

ARTICLE INFO

Keywords:
Hyperspectral imaging
Disease detection
Grapevine trunk disease
Precision viticulture
pixel-based classification

ABSTRACT

Precise and reliable identification of specific plant diseases is a challenge within precision agriculture nowadays. This is the case of esca, a complex grapevine trunk disease, that represents a major threat to modern viticulture as it is responsible for large economic losses annually. The lack of effective control strategies and the complexity of esca disease expression make essential the identification of affected plants, before symptoms become evident, for a better management of the vineyard. This study evaluated the suitability of a near-infrared hyperspectral imaging (HSI) system to detect esca disease in asymptomatic grapevine leaves of Tempranillo red-berried cultivar. For this, 72 leaves from an experimental vineyard, naturally infected with esca, were collected and scanned with a lab-scale HSI system in the 900-1700 nm spectral range. Then, effective image processing and multivariate analysis techniques were merged to develop pixel-based classification models for the distinction of healthy, asymptomatic and symptomatic leaves. Automatic and interval partial least squares variable selection methods were tested to identify the most relevant wavelengths for the detection of esca-affected vines using partial least squares discriminant analysis and different pre-processing techniques. Three-class and two-class classifiers were carried out to differentiate healthy, asymptomatic and symptomatic leaf pixels, and healthy from asymptomatic pixels, respectively. Both variable selection methods performed similarly, achieving good classification rates in the range of 82.77-97.17% in validation datasets for either three-class or two-class classifiers. The latter results demonstrated the capability of hyperspectral imaging to distinguish two groups of seemingly identical leaves (healthy and asymptomatic). These findings would ease the annual monitoring of disease incidence in the vineyard and, therefore, better crop management and decision making.

1. Introduction

The potential yield of agricultural crops can be affected by different biotic and abiotic stress factors leading to a reduction in the quantity and quality of production. Global crop losses caused by pathogens and pests have been estimated to account for 17–30% of crop production (Savary et al., 2019). Precise control of plant diseases is, therefore, a demanding challenge within precision agriculture where new and innovative techniques are needed to cope with the forthcoming trends in the agricultural sector (Mahlein et al., 2012).

In the last decades, optical sensor technologies have been recognised as promising tools for non-invasive assessment of plant physiological status and for disease diagnosis and detection on different scales (Mahlein, 2016; Sankaran et al., 2010; West et al., 2003; Zhang et al.,

Abbreviations: HSI, hyperspectral imaging; GLRaV, grapevine leafroll associated virus; GTDs, grapevine trunk diseases; RGB, red, green, blue; UAV, unmanned aerial vehicle; HSI-NIR, near-infrared hyperspectral imaging; BBCH, Biologische Bundesanstalt, Bundessortenamt and Chemical industry; NIR, near-infrared; 2D, two-dimensional; MC, mean centering; SM, smoothing; MSC, multiplicative scatter correction; SNV, standard normal variate; 1st D, first derivative; 2nd D, second derivative; PCA, principal component analysis; PC, principal components; PLS-DA, partial least squares discriminant analysis; PLS, partial least squares; CV, cross-validation; LV, latent variables; CC, correctly classified; TP, true positive; TN, true negative; FN, false negative; FP, false positive; iPLS, interval partial least squares; VIP, variable importance in projection; SR, selectivity ratio; RMSECV, root mean squared error of cross-validation; VS, variable selection.

* Corresponding author.
E-mail address: ainara.lopez@unavarra.es (A. López-Maestresalas).

https://doi.org/10.1016/j.compag.2022.106863
Received 22 September 2021; Received in revised form 30 January 2022; Accepted 8 March 2022
Available online 14 March 2022

2019). Biochemical and biophysical alterations of plant tissue caused by biotic and abiotic stresses result in the modification of the optical properties of leaves that can be captured by these sensors (Mahlein, 2016). Thus, spectral characteristics derived from plant-light interactions can be assessed within a wide range of the electromagnetic spectrum, specifically, in the 350 to 2500 nm region where reflectance spectral information relates to the biochemical composition and internal structures of leaves (Ollinger, 2011).

Among optical sensors, hyperspectral imaging (HSI) has proven its potential in the evaluation of plant diseases (Lowe et al., 2017; Mahlein et al., 2018), providing a better understanding of plant-pathogen interactions. During infection and disease development, alterations in the structure and chemical composition of tissues occur, such as the appearance of chlorotic and necrotic tissue, the production of pathogen-specific toxins, or the presence of pathogen structures. As a result of these plant impairments, changes in the reflectance response also happen (Mahlein, 2016). Thus, providing both spectral and spatial information of the imaged object, HSI seems to be useful for the detection and quantification of diseases (Bock et al., 2010), as it allows a pixel-wise distribution of disease symptoms on the leaf surface.

HSI technology, linked to meaningful data analysis approaches, has recently been used for the assessment of different grapevine diseases. Hence, several studies have been conducted concerning the detection of grapevine leafroll associated virus (GLRaV) leaf symptoms (Bendel et al., 2020c; Gao et al., 2020; MacDonald et al., 2016) as well as of yellows (Bendel et al., 2020a). Detection of powdery mildew and downy mildew diseases on both leaves (Oerke et al., 2016) and bunches (Knauer et al., 2017; Pérez-Roncal et al., 2020) has also been investigated. Regarding grapevine trunk diseases (GTDs), studies using different sensor technologies have been carried out on the detection of esca leaf symptoms. Some examples include the use of RGB imaging (Rançon et al., 2019) and hyperspectral spectroradiometers (Junges et al., 2020, 2018) separately, as well as in combination (Al-Saddik et al., 2018), or unmanned aerial vehicle (UAV) multispectral imagery (Albetis et al., 2019; Bendel et al., 2020b; Di Gennaro et al., 2016).

Grapevine trunk diseases are one of the main reasons for vine decline in grape growing regions worldwide and represent a major threat to viticulture due to the significant economic losses they cause principally through reducing yields and grape quality, increasing crop management costs, and shortening the longevity of the vineyard (Fontaine et al., 2016a; Gramaje et al., 2018). They involve several xylem-inhabiting fungi able to infect the vines mainly via propagation material in nurseries or pruning wounds in vineyards, leading to wood discolouration and decay, leaf and berry symptoms and, eventually, to vine death (Bertsch et al., 2013; Fontaine et al., 2016b; Mondello et al., 2018). Among GTDs, Esca complex is the most prevalent in European and Mediterranean countries (Guerin-Dubrana et al., 2019). The increasing disease incidence and severity is attributed to different factors, such as vineyard intensification or changes in vine management and cultural practices. The lack of effective strategies and means of disease control has surely contributed to its spread, especially since the ban of sodium arsenite at the beginning of the 21st century in Europe, the sole available product known to be effective against esca (Gramaje et al., 2018; Graniti et al., 2000).

Esca is a disease complex, comprising several syndromes according to the vine age, environmental factors, the type of wood and foliar symptoms and the pathogens involved (Bertsch et al., 2013; Surico, 2009), mostly associated with vascular ascomycete fungi *Phaeomoniella chlamydospora* and *Phaeoacremonium aleophilum*, and the basidiomycete *Fomitiporia mediterranea*. External symptoms appear as either a chronic (mild) form or an acute (severe) form, the so-called apoplexy. The acute form is characterised by a sudden wilting of the entire vine or of several shoots, leading to the plant death within a short period (Lecomte et al., 2012; Mugnai et al., 1999). The chronic form is characterised by typical leaf symptoms, showing interveinal red or yellow discolouration and necrotic zones that produce a tiger-stripe pattern, which can affect one or several shoots of the vine canopy. Foliar symptoms may not be observed in every growing season, even if the infected vine appeared symptomatic in previous years, and their expression can be influenced by several environmental, cultural and genetic factors (Fischer and Peighami Ashnaei, 2019).

The effects of Esca on vine morphology and physiology that have been shown to occur include modifications in the primary and secondary metabolism of leaves as symptoms progress (Fontaine et al., 2016b; Martín et al., 2019). These changes entail a decline of photosynthetic activity, alteration of carbohydrate metabolism, induction of defence responses (gene and protein expression), as well as alteration of phenolic compounds. Since these alterations at the cellular level of leaves arise prior to the development of visible symptoms (Fontaine et al., 2016b), a technique capable of detecting affected vines before symptoms become evident would enable annual monitoring of disease incidence in the vineyard and, therefore, better crop management and decision making.

The present study focuses on the suitability of applying near-infrared hyperspectral imaging (HSI-NIR) for the detection of esca disease complex in asymptomatic leaves of Tempranillo red-berried cultivar on a laboratory scale. For this purpose, effective image processing and multivariate data analysis techniques were merged to (1) develop classification models for the differentiation of healthy, asymptomatic and symptomatic leaves, and (2) identify the most relevant wavelengths for the detection of esca-affected vines.

2. Material and methods

2.1. Leaf samples

All grapevine leaves included in the experiment were collected close to 2018 harvest (September 20), at stage 89 according to the BBCH scale (Meier, 2001), from an experimental rainfed vineyard naturally infected with esca located in Olite, Spain (42°26′19.06″ N, 1°38′52.57″ W), which belongs to the Viticulture and Enology Station of Navarra (EVENA). This vineyard consisted of *Vitis vinifera* L. cv. 'Tempranillo' grafted on 110-Richter rootstock, originally planted in 1990. In this vineyard rows were oriented along the north–south axis, and featured row and vine spacing of 2.8 m and 1.4 m, respectively. Vines were trained to a 12-bud bilateral Royat Cordon system with vertical shoot orientation and managed according to conventional viticulture practices.

In this vineyard, the appearance of esca foliar symptoms had been systematically monitored from 2014, which allowed us knowing, for each individual plant, if esca had appeared before or not. Considering this historic recording that comprised five consecutive seasons, it was possible to collect leaves that fell into three categories: control (CO), asymptomatic leaves from vines that had never shown esca symptoms and could therefore considered to be totally healthy; asymptomatic leaves from plants were showing esca symptoms, named Esca 1 (E1), and symptomatic leaves from the same esca-affected vines considered for E1, named Esca 2 (E2). Twenty-four leaves of each category, 72 in total, were taken from no more than 6 different vines, always considering mature but not senescent leaves. Leaves were kept refrigerated (3 °C) until the measurement process started, around 24 h after the sample gathering.

2.2. Hyperspectral image acquisition and processing

The spectral imaging data used in this study were captured using a line scan HSI system composed of a Xeva 1.7–320 InGaAs camera (Xenics, Leuven, Belgium), with a resolution of 320 × 256 pixels in the 900–1700 nm spectral range (3.14 nm spectral resolution), coupled to an ImSpector N17E spectrograph (Specim, Spectral Imaging Ltd., Oulu, Finland) with a 30 μm slit and a 16 mm C-mount lens (f/1.4). The system also consisted of a linear translation stage driven by a stepper motor (LEFS25, SMC Corporation, Tokyo, Japan) attached to a black sample

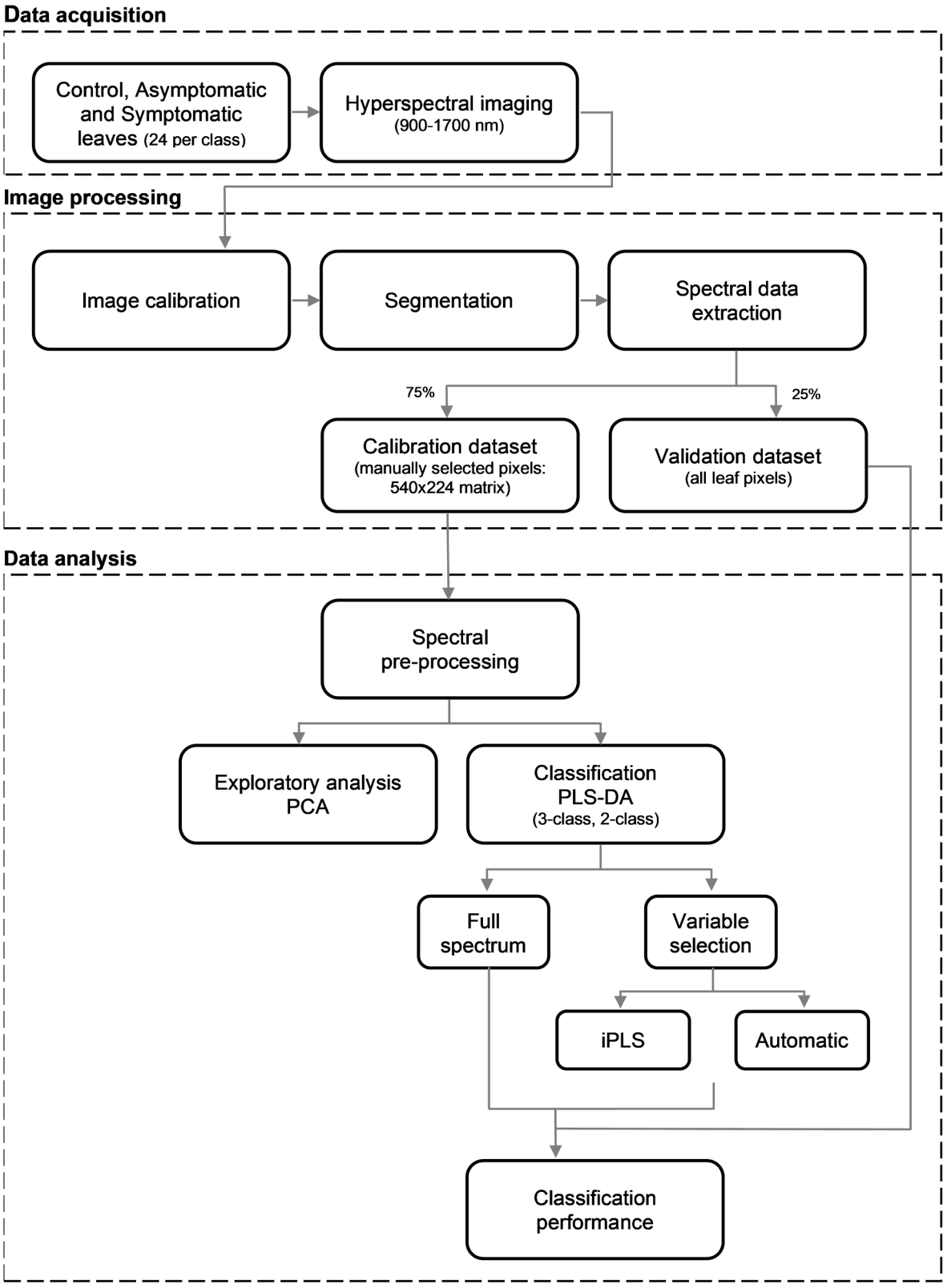

Fig. 1. Workflow of HSI analysis for the detection of esca disease complex.

holder plate, that allowed sample movement during image acquisition. Four 46 W halogen lamps pointing at the scanning area and a black cover enclosing the entire setup were used to ensure uniform lighting of the scene and to avoid interference from external light. A computer equipped with Xeneth 2.5 and ACT Controller software was used to adjust configuration settings and control the camera and translation stage during scanning, as well as to store the leaf images. The parameters of the system were optimised so that the free distance from lens to linear translation stage was set to 400 mm providing an image spatial resolution of 0.75 mm/pixel along the scanning line (320 pixels). The vendor's

calibration package was applied for image correction and the integration time was adjusted to 2 ms to avoid detector saturation.

Leaves were positioned with the adaxial side facing the camera and one hyperspectral image was taken per sample. RGB images as reference were also obtained for each sample by a Lumix DMC-TZ25 digital camera (Panasonic, Japan). In addition, maximum and minimum reflectance images were acquired for reflectance calibration, using a Teflon white calibration tile with standard reflectance of 99% (Specim, Spectral Imaging Ltd., Oulu, Finland) for the white reference and, with the lens covered and lights off for the dark reference.

The processing of NIR hyperspectral images was carried out using MATLAB R2018b (The MathWorks, Natick, MA, USA). The workflow of such images was as follows:.

- Image calibration. The raw intensity values were converted into relative reflectance values R(x,λ) as:

$$R(x,\lambda) = \frac{I_{Raw}(x,\lambda) - I_D(x,\lambda)}{I_W(x,\lambda) - I_D(x,\lambda)} \quad (1)$$

where × represents a pixel, λ represents a wavelength and I_{Raw}, I_D, and I_W are the intensity for the original image, the dark reference and the white reference images, respectively. Note that I_W is, at each pixel and wavelength, the 99% of the reference intensity on the white reference panel.

- Segmentation. The images were segmented using the algorithm in Lopez-Molina et al. (2017), which was aimed to discriminate the vegetal area from the background. This algorithm creates an initial superpixel-based oversegmentation, built upon local contrast measurements based on Baddeley's metrics. Superpixel images, introduced by Ren and Malik (2003), are oversegmented images such that each local granule is composed of contiguous pixels with similar features. The binarization of the superpixel image into a binary image is performed using Otsu threshold determination algorithm (Otsu, 1979) and basic morphological operations (which are meant to regularise the selected area and avoid isolated positive/negative detections). Some images contained small, yet relevant regions in which spectral measurements were saturated. In this regard, all pixels having at least 2% of the bands in maximum values were considered as saturated and hence removed from the selected area. Moreover, a low signal-to-noise ratio was observed at the beginning of the spectrum, resulting in noisy images in this region. Therefore, bands in the 900–1000 nm range were completely excluded for further analysis, reducing the spectral range to 1000–1700 nm with a total of 224 bands.
- Spectral data extraction. In this study, data were treated on a spectral basis. That is, each pixel (spectrum) was considered as an individual instance belonging to each of the abovementioned classes. This was achieved unfolding the three-dimensional hypercube into a 2D data matrix containing the leaf pixel reflectance values at the 224 wavelengths (from 1000 to 1700 nm).

The dataset was randomly divided into calibration and validation subsets. The former comprised 54 leaves (75% of the dataset, with equal presence of all classes), while the latter consisted of 18 leaves (25%). For each of the 54 leaves (18 images per class) in the calibration set, 10 pixels were manually selected using the graphical user-friendly interface HYPER-Tools (Mobaraki and Amigo, 2018) and taking the RGB images as a reference to identify and locate visually healthy and symptomatic leaf zones (avoiding nerves). For CO and E1 classes, pixels were selected from both internal and external zone leaf rings (5 pixels per ring), while for class E2 only the pixels corresponding to leaf zones with visible esca symptoms were selected. This supervised subselection of data resulted in a matrix (540 rows × 224 columns) used as the calibration dataset for the (classification) model training. The remaining 18 images (6 samples per class) were used as validation dataset.

2.3. Multivariate data analysis

The multivariate data analysis was carried out using the PLS_Toolbox version 8.8 (Eigenvector Research Inc., Wenatchee, WA, USA) within MATLAB® computational environment. The workflow of this study, including the steps of data acquisition, image processing and data analysis, is illustrated in Fig. 1.

2.3.1. Spectral pre-processing

Hyperspectral data contain complex and substantial information, often affected by undesirable phenomena such as physical effects or noise. Thus, mathematical pre-processing is normally used to mitigate the effects of irregularities in the spectra and consequently improve the data analysis (exploratory analysis and multivariate models) (Rinnan et al., 2009). In this study, different pre-processing techniques were tested to correct light scattering and noise effects, and to remove baseline drifts and overlapping peaks in the spectra (Nicolaï et al., 2007; Rinnan et al., 2009). These included mean centering (MC), smoothing (SM), multiplicative scatter correction (MSC (mean)), standard normal variate (SNV), and first and second derivatives (1st D and 2nd D, respectively). Smoothing was performed using a 15-point Savitzky–Golay (Savitzky and Golay, 1964) filtering operation, while derivatives were computed using the Savitzky–Golay method by a second-order polynomial and 15 window points. The pre-processing techniques were evaluated both individually and combined with posterior mean centering, in order to enhance the performance of the classification model. The effect of no pre-processing (None) was also analysed. A total of 12 pre-processing combinations were tested.

2.3.2. Exploratory data analysis

A principal component analysis (PCA) was carried out for exploratory purposes and to visualise any difference between the three classes (CO, E1 and E2) in the calibration dataset. PCA is a dimensionality reduction technique that transforms the original variables of a dataset into a set of new uncorrelated variables, known as principal components (PC), while retaining most of the existing variability (Jolliffe, 1986). One PCA per pre-processing combination was conducted in this study and its interpretation was based on the information retained in both the PC score and loading line plots.

2.3.3. Data classification

Partial least squares discriminant analysis (PLS-DA) was used to classify grapevine leaves according to the expression of esca leaf symptoms. For this, three-class classifiers were developed to differentiate healthy (CO), asymptomatic (E1) and symptomatic (E2) leaf pixels, as well as two-class classifiers to distinguish two apparently healthy leaf types (CO and E1 pixels) before symptoms become visible. PLS-DA is a supervised technique based on the PLS regression algorithm that predicts class membership on a dataset by maximising the covariance between the categorical Y matrix and the data matrix X (the leaf pixel spectral matrix) (Barker and Rayens, 2003). In this study, PLS-DA models were calculated on a calibration data matrix of size 540 × 224 and 360 × 224 for three-class and two-class classifiers, respectively. A single Venetian blinds cross-validation (CV) (10 data splits) method was used to select the optimal number of latent variables (LV). As in the case of PCA analysis, one PLS-DA model was conducted for each of the pre-processing techniques tested.

In order to identify a subset of relevant spectral variables that preserve the most variability, while reducing the dimensionality of

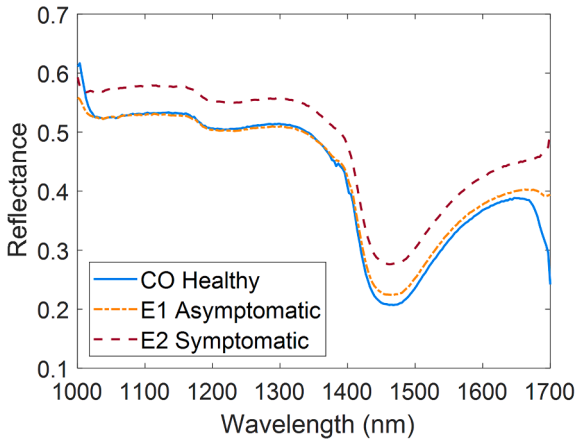

Fig. 2. Mean reflectance spectra (1000–1700 nm) of healthy, asymptomatic and symptomatic esca leaf samples in the calibration set. Mean spectrum corresponds to the average of n = 180 pixels of characteristic tissue of each class.

hyperspectral data and improving model interpretation, 2 variable selection methods were applied for the three-class and two-class classifiers: automatic and interval PLS (iPLS). The automatic method conducts variable selection using both variable importance in projection (VIP) (Chong and Jun 2005) and selectivity ratio (SR) (Rajalahti et al., 2009) approaches and only returns the selection leading to the lowest root mean squared error of cross-validation (RMSECV). In each run, the variables with the lowest VIP or SR measured values are removed, and the iteration stops when no improvement in the model performance is achieved. The iPLS develops local PLS regression models on equidistant subintervals of the full spectrum region and selects a subset of variables that provide superior prediction (lowest RMSECV) compared to using the full spectrum (Nørgaard et al., 2000). In forward iPLS the algorithm conducts a sequential search for the best variable or combination of variables where intervals are successively included in the analysis. In this study, the automatic method was applied for the same pre-processing combinations as in the full spectrum models and the forward iPLS for the best performing pre-processing using an automatic number of intervals with interval size between 10 and 20 (in increments of 2 wavelengths, i.e., 10, 12, 14, 16, 18, 20).

The validation dataset (leaf pixel matrices of the remaining 6 images per class) was then employed for the independent external validation of the best performing PLS-DA models with and without variable selection, for each classification case. A classification image was generated per leaf based on the pixel membership prediction for each sample, showing the predictable esca-affected areas.

The performance of the PLS-DA models was assessed by the overall classification accuracy, the percentage of correctly classified (% CC) pixels, and the sensitivity and specificity of each class obtained in CV. Classification accuracy and class sensitivity and specificity parameters were calculated as follows (Ballabio and Consonni, 2013):.

$$Accuracy = \frac{TP + TN}{TP + TN + FN + FP} \times 100\% \quad (2)$$

$$Sensitivity = \frac{TP}{TP + FN} \quad (3)$$

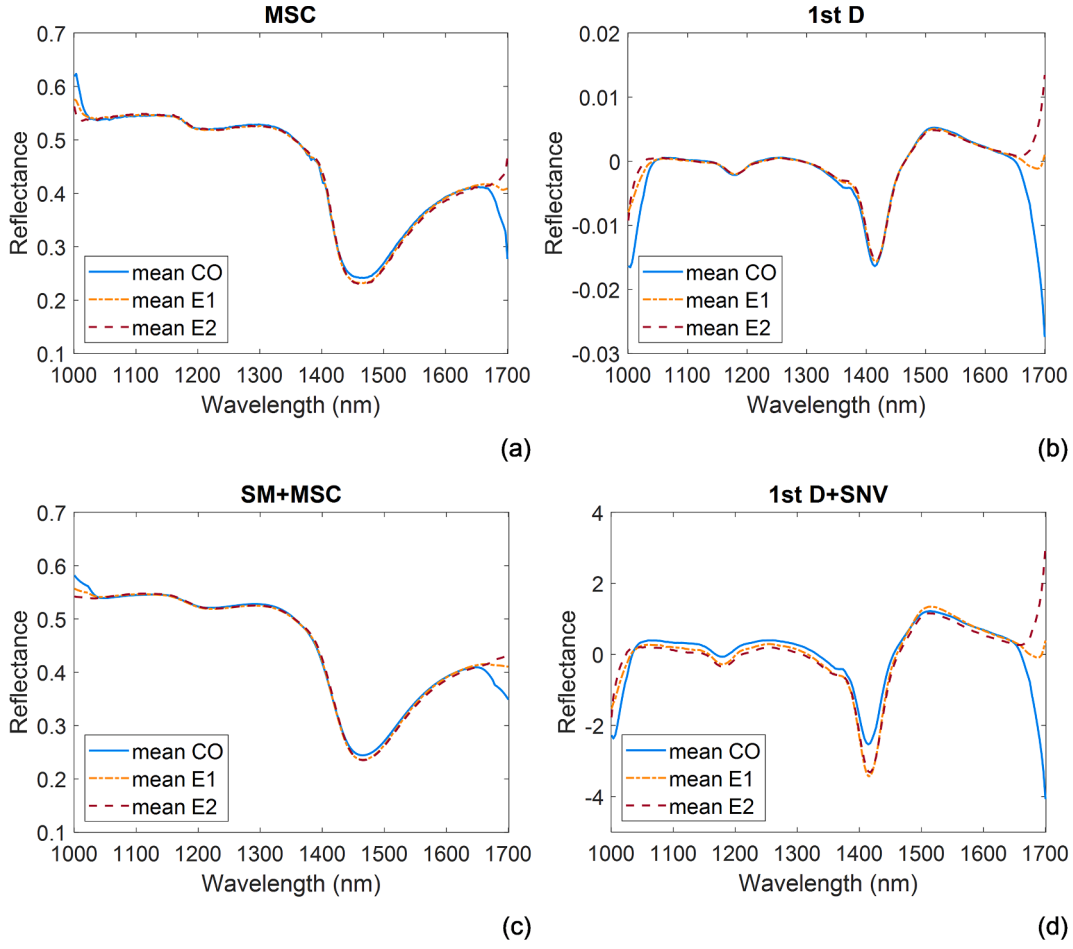

Fig. 3. Mean pre-processed spectra of the calibration dataset: (a) MSC; (b) 1st derivative; (c) Smoothing and MSC; (d) 1st derivative and SNV.

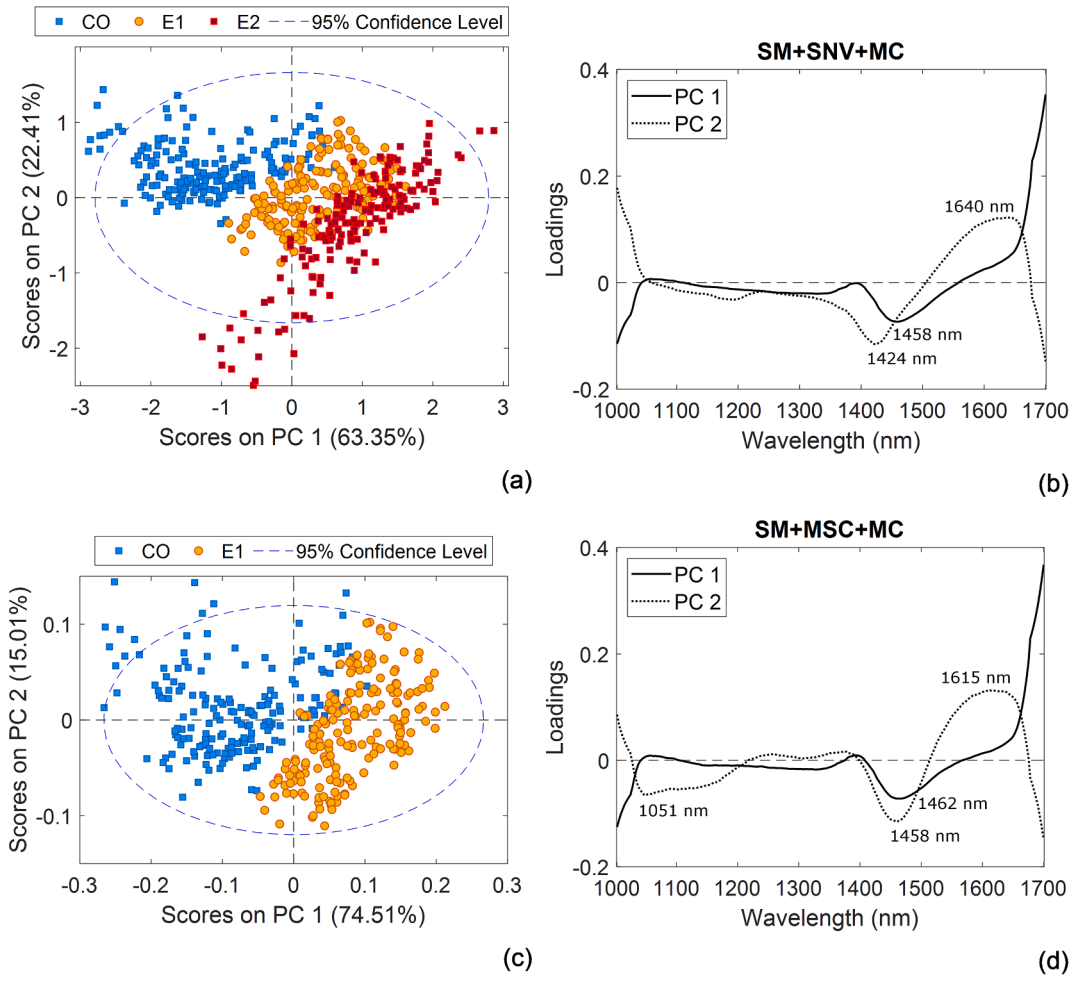

Fig. 4. PCA results for the best data pre-processing combination for class separation in the calibration dataset: (a) score plot of PC1 vs. PC2 for the three-class analysis using SM + SNV + MC pre-processing; (b) loadings for PC1 and PC2 for the three-class analysis; (c) score plot of PC1 vs. PC2 for the two-class analysis using SM + MSC + MC pre-processing; (d) loadings for PC1 and PC2 for the two-class analysis.

$$Specificity = \frac{TN}{TN + FP} \quad (4)$$

where TP, TN, FN and FP indicate the number of true positive, true negative, false negative and false positive pixels, respectively. For an adequate performance, the accuracy should be close to 100% and the sensitivity and specificity close to 1. Moreover, the percentage of correctly predicted pixels per class obtained on each sample was used to the external validation assessment.

3. Results and discussion

3.1. Spectra interpretation and pre-processing

Mean reflectance spectra of the healthy (CO), asymptomatic (E1) and symptomatic (E2) pixels selected in the calibration dataset are shown in Fig. 2. A similar trend in the spectral signature was observed for the three leaf classes along the selected spectral range (1000–1700 nm). The

Table 1
Summary results of the CV dataset for the best performing three-class (healthy vs. asymptomatic vs. symptomatic pixel-based) and two-class (healthy vs. asymptomatic pixel-based) PLS-DA models using different pre-processing combinations.

Pre-Processing	n	λ	LV	Variance (%)	CO (%CC)	E1 (%CC)	E2 (%CC)	Accuracy (%)
None	540	224	4	99.97	95.00	76.11	98.33	89.81
SM + MC	540	224	5	99.83	93.89	77.78	80.00	83.89
1st D + MC	540	224	3	94.20	95.56	60.00	92.78	82.78
SM + SNV + MC	536	224	5	96.51	94.44	78.89	85.23	86.19
SM + 1st D + MC	535	224	2	91.30	90.56	68.33	96.00	84.86
1st D + SNV + MC	538	224	4	95.34	94.44	73.33	87.08	84.94
None	360	224	3	99.97	90.56	98.33	–	94.44
SM + MC	359	224	4	99.49	91.62	96.11	–	93.87
1st D + MC	360	224	3	94.92	92.78	96.67	–	94.72
SM + MSC + MC	358	224	4	95.80	94.97	96.09	–	95.53
SM + 1st D + MC	360	224	2	91.21	90.56	98.33	–	94.44
1st D + SNV + MC	359	224	3	92.75	95.00	95.53	–	95.26

n: number of samples used; λ: number of wavelengths; LV: latent variables selected; CO: healthy sample; E1: asymptomatic sample; E2: symptomatic sample; CC: correctly classified.

Table 2
Summary results of the CV dataset for the best performing three-class (healthy vs. asymptomatic vs. symptomatic pixel-based) and two-class (healthy vs. asymptomatic pixel-based) PLS-DA models using different pre-processing and variable selection methods.

VS	Pre-Processing	n	λ	LV	Variance (%)	CO (%CC)	E1 (%CC)	E2 (%CC)	Accuracy (%)
Auto	None	471	80	3	99.96	88.70	75.00	96.61	85.56
Auto	SM + MC	476	116	5	99.79	92.35	75.57	80.00	82.77
Auto	SM + MSC + MC	466	99	4	98.31	96.45	73.14	84.43	84.55
Auto	1st D + SNV + MC	492	216	4	96.24	95.98	71.76	86.49	84.76
iPLS-20*	None	471	120	3	99.97	94.92	78.41	89.83	87.47
iPLS-10*	SM + SNV + MC	483	30	2	98.49	91.28	70.86	94.85	84.89
Auto	None	336	48	3	99.95	92.68	98.26	–	95.54
Auto	SM + MC	336	123	4	99.56	89.41	98.19	–	93.75
Auto	1st D + MC	336	137	4	97.31	96.41	97.04	–	96.73
Auto	SM + SNV + MC	331	116	2	93.84	91.46	98.80	–	95.17
iPLS-14*	None	336	70	3	99.96	90.85	98.84	–	94.94
iPLS-10*	SM + MSC + MC	332	50	3	97.11	96.36	97.60	–	96.99

VS: variable selection; n: number of samples used; λ: number of wavelengths; LV: latent variables selected; CO: healthy sample; E1: asymptomatic sample; E2: symptomatic sample; CC: correctly classified; Auto: automatic; iPLS-*: interval partial least squares (*: interval size).

mean spectra indicated differences in the magnitude of reflectance between the classes, being the reflectance values of class E2 higher than those of classes E1 and CO. Furthermore, the greatest difference between classes was observed in the 1400–1700 nm range related to the water content and leaf biochemicals (Fourty et al., 1996), in which a reflectance valley was noticeable around 1450 nm due to O-H stretching first overtone (Osborne et al., 1993). Leaves suffering from increased tissue dehydration show a general increase in reflectance throughout the 400–2500 nm region due to alterations in the internal leaf structure (associated with increased cell air spaces, among others) (Carter, 1991; Gausman, 1974). The higher reflectance obtained for E2 pixels within the whole spectral range would be in agreement with this statement as these values corresponded to necrotic tissue or areas showing some desiccation in symptomatic leaves. Thus, morphological and physiological changes caused by the disease led to a different spectral response in symptomatic leaves compared to asymptomatic and healthy ones.

NIR reflectance spectra presented variations and spectral noise besides sample information due to instrumental noise and light scattering from the internal leaf structure. Fig. 3 displays the effects of some of the denoising and scatter corrective pre-processing techniques used to reduce these phenomena in the spectra. The algorithm MSC (mean) corrects for the scatter variability (Fig. 3a), and the SM + MSC combination also removes the noise effects (Fig. 3c). Savitzky-Golay 1st derivative eliminates the effect of baseline drifts in the spectra (Fig. 3b), and the 1st D + SNV combination also removes multiplicative scatter effects (Fig. 3d).

3.2. Exploratory data analysis: PCA

In order to explore the spectral variation of the three leaf classes in the calibration dataset, PCA was used for each combination of pre-processing techniques. In the case of three-class analysis, the best class segregation was accomplished after applying SM + SNV + MC pre-processing combination, where 5 PCs were selected accounting for 97.28% of the variance (3 outliers removed). Fig. 4a displays PC1 (63.35%) vs. PC2 (22.41%) scores, revealing a slight distinction in the cross-sectional direction of the three groups in the dataset with some overlap, mainly between asymptomatic and symptomatic samples. Moreover, nearly all healthy pixels presented negative values in the first component and could be roughly separated from E1 and E2 pixels along it. The PC1 and PC2 loading plot (Fig. 4b) showed interpretable bands at 1458 nm (negative) in PC1, and at 1424 nm (negative) and 1640 nm (positive) in PC2. The bands at 1424 nm and 1458 nm (O-H stretch first overtone) are related with phenol groups (ArOH) and water absorption, respectively. The band at 1640 nm could be associated with the C-H stretch first overtone (Osborne et al., 1993).

Regarding the two-class analysis, the SM + MSC + MC combination was found to be the best data pre-processing for the separation of healthy and asymptomatic pixels. The first 5 PCs, accounting for 97.12% of the variance (1 outlier removed), were used to build the PCA. Fig. 4c displays the score plot of PC1 (74.51%) vs. PC2 (15.01%) showing that healthy and asymptomatic samples could almost be separated along the PC1. The loading plot of these first 2 PCs (Fig. 4d) showed interpretable bands at 1462 nm (negative) in PC1, and at 1051 nm (negative), 1458 nm (negative) and 1615 nm (positive) in PC2. The bands at 1051 nm and 1615 nm (C-H stretch first overtone) could be related with methylene groups (CH_2 and $=CH_2$, respectively). The band at 1462 nm is associated with the N-H stretch first overtone found in amide groups ($CONH_2$), and the band at 1458 nm is related with the absorption of water (Osborne et al., 1993).

3.3. Data classification: PLS-DA and variable selection performance

In this study, 12 PLS-DA models (using the 1000–1700 nm spectrum) were developed for the distinction of esca leaf symptoms, for both three-class and two-class classifiers, applying the same pre-processing combinations as in PCA. Table 1 summarises the results of the 6 best performing PLS-DA models (including the effect of no pre-processing) for each classification case in terms of overall accuracy and percentage of correctly classified (% CC) pixels of each class obtained in the CV dataset. Accuracy values above 82% and 93% were obtained for three-class and two-class classifiers, respectively, regardless of the pre-processing combination applied.

In three-class models, better classification rates were achieved for classes CO and E2 (80–99% CC) than for class E1 (60–79% CC), with most of the misclassified pixels in the latter being assigned as

Table 3
Sensitivity and specificity values obtained in the CV dataset for the best three-class PLS-DA model with and without variable selection.

				Sensitivity			Specificity		
VS	Pre-Processing	n	λ	CO	E1	E2	CO	E1	E2
None	SM + SNV + MC	536	224	0.978	0.856	0.938	0.949	0.579	0.883
iPLS-10*	SM + SNV + MC	483	30	0.965	0.869	0.963	0.958	0.740	0.841

VS: variable selection; n: number of samples used; λ: number of wavelengths; CO: healthy sample; E1: asymptomatic sample; E2: symptomatic sample; iPLS-*: interval partial least squares (*: interval size).

Table 4
Sensitivity and specificity values obtained in the CV dataset for the best two-class PLS-DA model with and without variable selection.

				Sensitivity		Specificity	
VS	Pre-Processing	n	λ	CO	E1	CO	E1
None	SM + MSC + MC	358	224	0.950	0.961	0.961	0.950
iPLS-10*	SM + MSC + MC	332	50	0.964	0.976	0.976	0.964

VS: variable selection; n: number of samples used; λ: number of wavelengths; CO: healthy sample; E1: asymptomatic sample; iPLS-*: interval partial least squares (*: interval size).

symptomatic (15–32%). Despite the fact that better accuracy was obtained with no pre-processing (89.81%), the SM + SNV + MC combination was selected as the best performing PLS-DA model since the % CC pixels for E1 class was higher (78.89% CC vs. 76.11%), and also the accuracy was better (86.19%) than with the other models. Concerning two-class models, best results were achieved when applying SM + MSC + MC pre-processing combination with classification rates around 95% of both accuracy and % CC pixels of each class (see Table 1).

The results of the best performing PLS-DA models using automatic and forward iPLS variable selection methods are shown in Table 2. A robust PLS (alpha value equal to 0.9) was computed for automatic outlier detection resulting in a large sample removal. In general, a greater variable reduction (fewer feature wavelengths selected) was performed with forward iPLS.

For three-class classifiers, classification rates similar to those of models without variable selection were obtained, for the same pre-processing combinations in the case of automatic method and for the best performing pre-processing algorithm using different interval sizes in iPLS. Although a higher accuracy was obtained with no pre-processing (87.47%), the SM + SNV + MC combination using forward iPLS (interval size of 10) achieved better classification (overall accuracy increase of 10%) and spatial location of pixels in the validation samples (with fewer wavelengths) and was therefore selected for external validation. In this model, 2 LVs (accounting for 98.49% of the variance) and 30 wavelengths (covering the 1596–1687 nm range) were chosen for the three-class distinction.

In two-class classifiers, classification results improved when variable selection methods were applied. As in the full spectrum model, the highest results were obtained for SM + MSC + MC pre-processing, using forward iPLS (interval size of 10), which resulted in classification rates

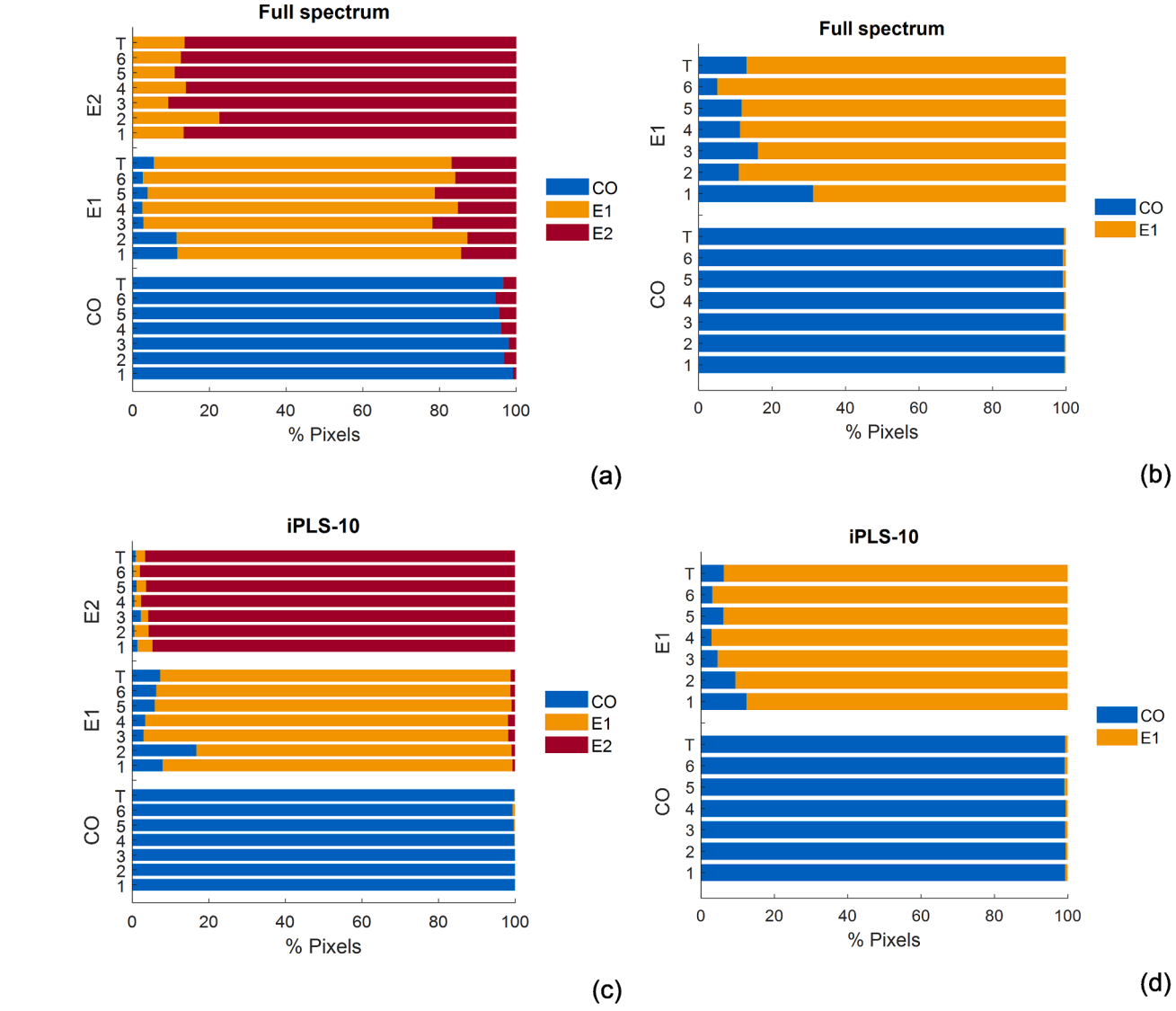

Fig. 5. Percentage of predicted pixels per class (CO, E1 and E2) obtained in the validation dataset (sample 1 to 6 of each class and total (T) per class): (a) three-class full spectrum model using SM + SNV + MC pre-processing; (b) two-class full spectrum model using SM + MSC + MC pre-processing; (c) three-class iPLS-10 model using SM + SNV + MC pre-processing; (d) two-class iPLS-10 model using SM + MSC + MC pre-processing.

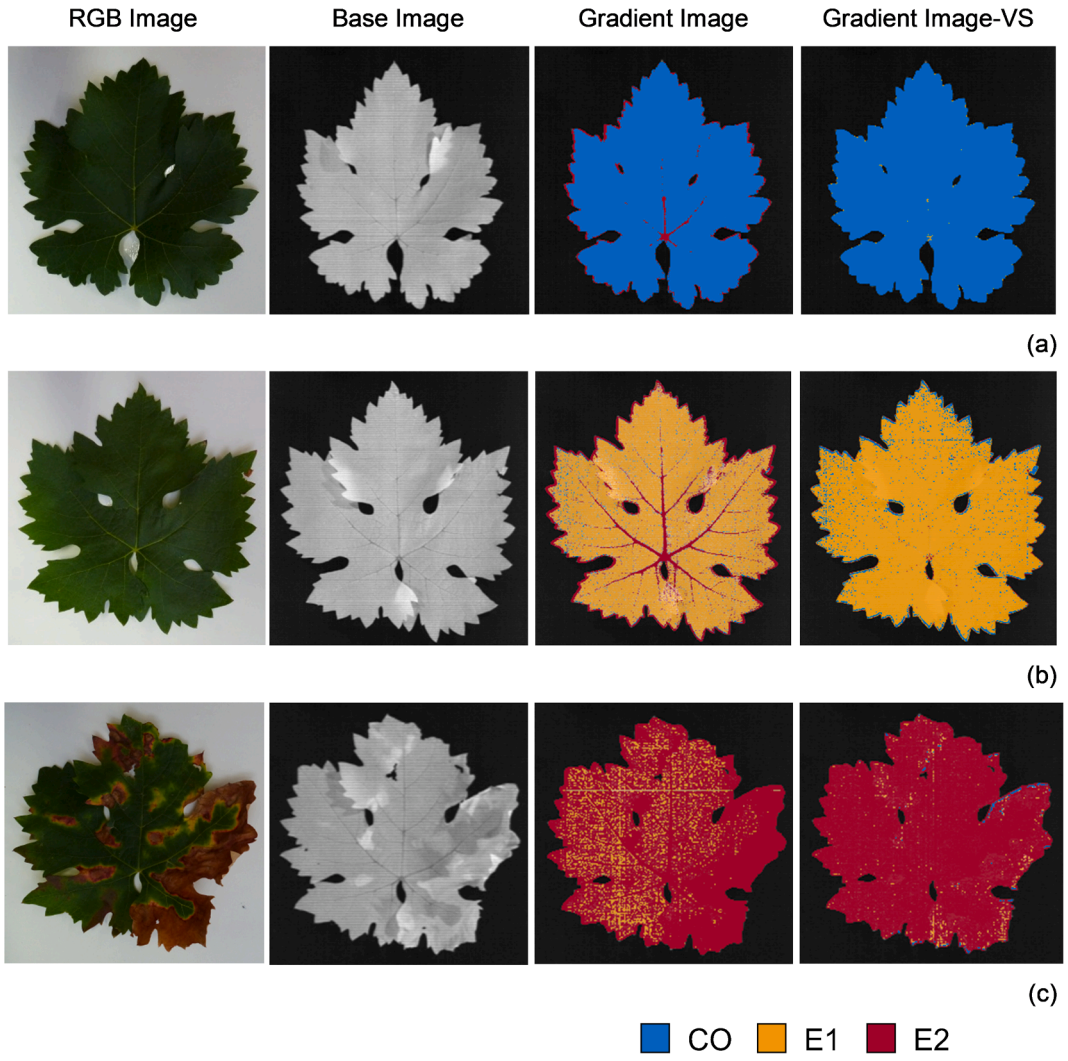

Fig. 6. Display of a pixel-based classification in the external validation using SM + SNV + MC three-class PLS-DA models for samples: (a) CO (healthy sample 5); (b) E1 (asymptomatic sample 6); and (c) E2 (symptomatic sample 4). Images from left to right correspond to: RGB images taken as reference, greyscale base reflectance images at 1260 nm used for displaying the prediction results, and gradient reflectance images of the probability-based classification of pixels obtained from the full spectrum and iPLS (VS) models, respectively.

above 96%. For this combination, 3 LVs (97.11% of variance explained) and 50 wavelengths (covering the 1000–1029 nm, 1126–1154 nm, 1408–1436 nm, 1534–1562 nm and 1659–1687 nm ranges) were chosen to build the classification model. This was selected as the best performing PLS-DA model for the two-class distinction and hence the one used for the external validation.

These characteristic spectral ranges identified for the leaf classes differentiation would be related to the changes in the biochemical composition of leaves, which are caused by the effect of esca on the vine physiology as stated previously, leading to the alteration of the spectral response. Thus, absorption features related to leaf constituents could be found near 1020 nm and 1420 nm associated to nitrogen status and lignin, respectively (Serrano et al., 2002); near 1143 nm assigned to aromatic structure and methyl group (CH_3) and at 1540 nm related to starch content (Fourty et al., 1996; Osborne et al., 1993); and near 1660 nm attributed to phenolic compounds (Kokaly and Skidmore, 2015).

Table 3 shows the sensitivity and specificity values of each class obtained for the best performing three-class model, with and without variable selection, which in both cases included the SM + SNV + MC pre-processing combination. Higher values were achieved after wavelength selection (except for CO sensitivity and E2 specificity) and, in both models, the CO and E2 classes obtained better sensitivity and specificity values than E1 class. This means that CO and E2 pixels were better classified into their corresponding class than E1 pixels. Furthermore, misclassified pixels in CO and E2 classes (5.55–8.72% and 5.15–14.77%, respectively) were assigned as E1 class, resulting in a specificity value decrease for the latter.

In Table 4, sensitivity and specificity values of both CO and E1 classes obtained for the best performing model with and without variable selection are displayed. As in three-class classifiers, the model with variable selection obtained better values. In this case, sensitivity was slightly higher for E1 class than for CO one, indicating that E1 pixels were better classified than CO pixels (97.60% CC vs. 96.36%).

The external validation of the three-class classifier was performed independently for each sample of the validation dataset (18 leaves). For this, only the PLS-DA models using SM + SNV + MC pre-processing with variable selection (iPLS-10, 6th row of Table 2) and without it (4th row of Table 1) were used. As can be seen in Fig. 5a and c, a large proportion of pixels (above 74%) in all samples were correctly classified into the class they belonged to. Higher classification rates were achieved for healthy and symptomatic pixels than for asymptomatic pixels as in the case of the CV dataset, and also the results improved after wavelengths selection. In total, 96.64% and 99.78% of pixels from the 6 CO leaves were correctly classified as healthy, 77.60% and 91.57% of pixels from

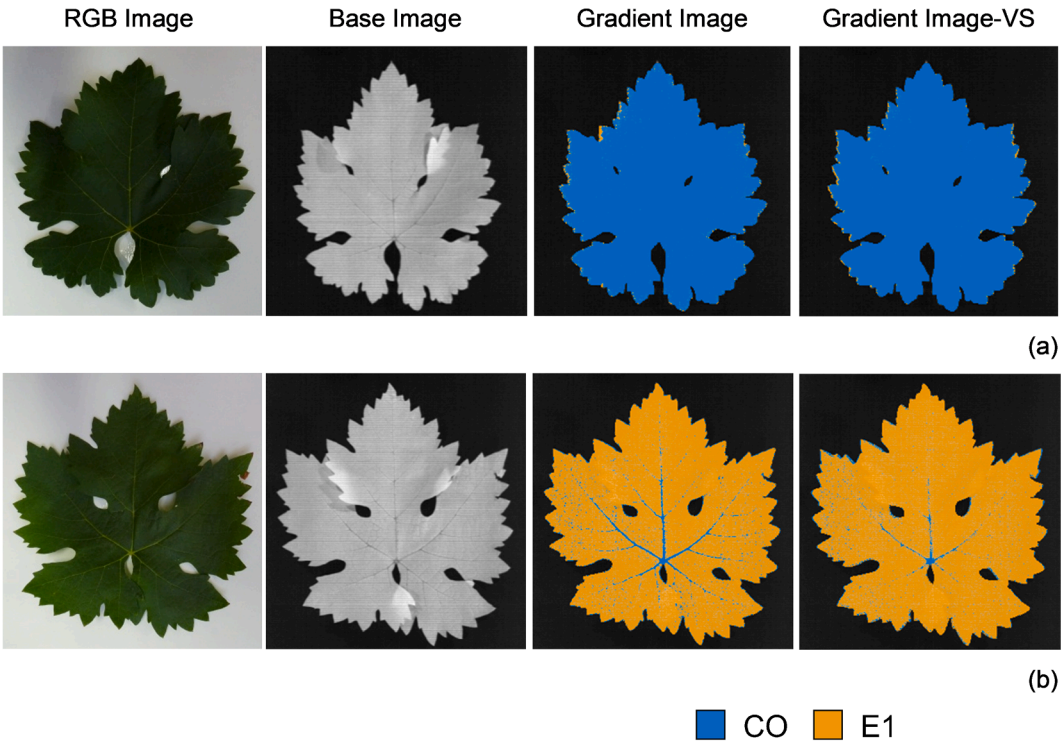

Fig. 7. Display of a pixel-based classification in the external validation using SM + MSC + MC two-class PLS-DA models for samples: (a) CO (healthy sample 5); and (b) E1 (asymptomatic sample 6). Images from left to right correspond to: RGB images taken as reference, greyscale base reflectance images at 1260 nm used for displaying the prediction results, and gradient reflectance images of the probability-based classification of pixels obtained from the full spectrum and iPLS (VS) models, respectively.

the 6 E1 leaves were correctly labelled as asymptomatic, and 86.47% and 96.67% of pixels from the 6 E2 leaves were identified as symptomatic, for the model using the full spectrum (Fig. 5a) and the iPLS (Fig. 5c), respectively.

Fig. 6a-c displays a pixel-based classification using the best three-class PLS-DA models mentioned above for 3 leaves of the validation dataset belonging to classes CO (sample 5), E1 (sample 6) and E2 (sample 4), respectively. In sample CO (Fig. 6a) 95.65% and 99.62% of pixels were correctly assigned as healthy; in sample E1 (Fig. 6b) 81.47% and 92.56% of pixels were labelled as asymptomatic; and in sample E2 (Fig. 6c) 86.14% and 97.66% of pixels were classified as symptomatic, for the full spectrum and iPLS models, respectively. In general, as seen in Fig. 6 the misclassified pixels were mostly located on the edge and leaf nerves, especially in CO and E1 leaves (Fig. 6a and b) for the model without variable selection (Gradient image), and on the sloping surfaces of the leaf, mainly on E2 leaf margins showing necrotic tissue (Fig. 6c). Moreover, a greater differentiation within the leaf (nerves, necrotic zones, internal areas and edges) was observed when using the full spectrum model, which allowed to distinguish asymptomatic areas (more orange pixels) from symptomatic ones (higher concentration of magenta pixels) on leaf E2 (Fig. 6c). However, almost all leaf pixels in the three classes corresponded to their class when the variable selection method was used, which suggests that esca caused effects produce a different spectral response in the three leaf types and, therefore, at these selected wavelengths an easier discrimination between healthy, asymptomatic and symptomatic classes is achieved.

Regarding the external validation of CO and E1 leaves for the two-class distinction (12 samples), only the PLS-DA models using SM + MSC + MC pre-processing with variable selection (iPLS-10, 12th row of Table 2) and without it (10th row of Table 1) were used. In most samples, a large proportion of pixels (above 83%) were correctly assigned into their corresponding class as shown in Fig. 5b and d. Higher classification rates were obtained for healthy pixels than for asymptomatic pixels and, in general, the results improved when variable selection was applied. In total, 99.39% and 99.27% of pixels from the 6 CO leaves were correctly classified as healthy, and 86.99% and 93.83% of pixels from the 6 E1 leaves were correctly labelled as asymptomatic, for the full spectrum (Fig. 5b) and iPLS (Fig. 5d) models, respectively.

Fig. 7a-b displays a pixel-based classification using the best two-class PLS-DA models mentioned above for the same 2 validation samples used in three-class distinction belonging to CO (sample 5) and E1 (sample 6) classes, respectively. For instance, in CO sample (Fig. 7a) 99.13% and 99.06% of pixels were correctly assigned as healthy (blue pixels), whereas in E1 sample (Fig. 7b) 94.96% and 96.96% of pixels were labelled as asymptomatic (orange pixels), for the full spectrum and iPLS models, respectively. As in the three-class model displays, misclassified pixels were located on the edge and leaf nerves, which was most appreciated for the full spectrum model (Gradient images on Fig. 7a and b). In any case, both models allowed to differentiate the two apparently healthy leaf classes (CO and E1 classes).

Overall, the results showed that the PLS-DA classifier performed very well in discriminating both three classes (healthy, asymptomatic and symptomatic) and two classes (healthy and asymptomatic) of leaves, which suggests the possibility of identifying esca-affected leaves before symptoms become evident using hyperspectral imaging. Similar results to the ones reported here have been obtained in other studies concerning the detection of disease symptoms on grapevine leaves. Junges et al. (2020) evaluated the potential of a hyperspectral sprectroradiometer to discriminate asymptomatic and symptomatic leaves of Merlot cultivar affected by GTDs and GLRaV. Based on the differences in the spectral signature they were able to distinguish between leaf types and identify the most useful wavelengths for the distinction task. Hyperspectral and multispectral imaging approaches for the detection of foliar Esca symptoms in Phoenix cultivar were investigated by Bendel et al. (2020b). Accuracy values above 70% were obtained for healthy, pre-symptomatic and symptomatic leaves differentiation based on spectral reflectance in the 1000–2500 nm range. Our study not only allows to differentiate whether a leaf is affected, but also a pixel-based

identification of disease symptoms on the leaf surface (mapping of esca-affected areas). Moreover, a successful distinction of two groups of leaves that are identical to the naked eye (healthy and asymptomatic) has been achieved. Thus, the results obtained in this study could lay the groundwork for the development of a decision support tool in the context of precision viticulture. However, for future investigations in this line of research, it would be interesting to compare the spectral response of other biotic and abiotic factors that may produce similar symptoms on leaves. In this study, the experimental set-up was specially designed to avoid the effects of other stresses, as all plants were under the same growing conditions. Therefore, it can be said with confidence that the differentiating factor was associated with the esca. In any case, diagnosis of the presence of esca causal agents in vines would be highly recommended to ensure that only this disease is being assessed and no other biotic or abiotic stresses.

4. Conclusions

The suitability of NIR hyperspectral imaging to discriminate esca-affected leaves according to foliar symptoms expression (healthy, asymptomatic and symptomatic leaves) was evaluated in this study. In general, accuracy values in the range of 82.78–95.53% were obtained in CV and validation datasets for both three-class and two-class PLS-DA classifiers, using the full spectrum and different pre-processing techniques. Similar and even better classification rates (82.77–97.17%) were achieved after variable selection, where both automatic and forward iPLS methods gave similar performances. Leaf reflectance measurements in the NIR region revealed useful information for the detection of foliar esca symptoms. Thus, wavelengths in the 1596–1687 nm range were identified as the most relevant ones for the three leaf classes distinction, while 5 spectral ranges (1000–1029, 1126–1154, 1408–1436, 1534–1562 and 1659–1687 nm) were selected for healthy and asymptomatic classes differentiation. Hyperspectral technology would therefore allow the detection of differential spectral characteristics of esca-affected leaves, even before the appearance of visible symptoms, which would be very useful for disease monitoring and vineyard management in a more accurate way. However, esca disease expression depends on several factors, including the cultivar and other biotic and abiotic determinants, and further research is needed to support these findings.

CRediT authorship contribution statement

Claudia Pérez-Roncal: Data curation, Formal analysis, Investigation, Methodology, Supervision, Validation, Visualization, Writing – original draft, Writing – review & editing. **Silvia Arazuri:** Conceptualization, Funding acquisition, Investigation, Project administration, Resources, Writing – review & editing. **Carlos Lopez-Molina:** Data curation, Formal analysis, Investigation, Methodology, Software, Supervision, Validation, Writing – original draft, Writing – review & editing. **Carmen Jarén:** Conceptualization, Resources, Writing – review & editing. **Luis G. Santesteban:** Conceptualization, Resources, Writing – review & editing. **Ainara López-Maestresalas:** Data curation, Investigation, Methodology, Supervision, Validation, Visualization, Writing – review & editing.

Declaration of Competing Interest

The authors declare that they have no known competing financial interests or personal relationships that could have appeared to influence the work reported in this paper.

Acknowledgements

This research was supported by Public University of Navarre post-graduate scholarships (FPI-UPNA-2017), by the Spanish Ministry of Economy and Competitiveness (AGL2017-83738-C3-1R, AEI/EU-FEDER), and by the Spanish Ministry of Science, Innovation and Universities (PID2019-108392GB-I00, AEI/10.13039/ 501100011033).

The authors would like to thank the Viticulture and Enology Station of Navarra-Spain (EVENA) for providing the samples and for their valuable support.

References

Al-Saddik, H., Laybros, A., Billiot, B., Cointault, F., 2018. Using image texture and spectral reflectance analysis to detect Yellowness and Esca in grapevines at leaf-level. Remote Sens. 10, 618. https://doi.org/10.3390/rs10040618.

Albetis, J., Jacquin, A., Goulard, M., Poilvé, H., Rousseau, J., Clenet, H., Dedieu, G., Duthoit, S., 2019. On the potentiality of UAV multispectral imagery to detect Flavescence dorée and grapevine trunk diseases. Remote Sens. 11, 23. https://doi.org/10.3390/rs11010023.

Ballabio, D., Consonni, V., 2013. Classification tools in chemistry. Part 1: linear models. PLS-DA. Anal. Methods 5, 3790–3798. https://doi.org/10.1039/C3AY40582F.

Barker, M., Rayens, W., 2003. Partial least squares for discrimination. J. Chemom. 17 (3), 166–173. https://doi.org/10.1002/cem.785.

Bendel, N., Backhaus, A., Kicherer, A., Köckerling, J., Maixner, M., Jarausch, B., Biancu, S., Klück, H.-C., Seiffert, U., Voegele, R.T., Töpfer, R., 2020a. Detection of two different grapevine yellows in Vitis vinifera using hyperspectral imaging. Remote Sens. 12, 4151. https://doi.org/10.3390/rs12244151.

Bendel, N., Kicherer, A., Backhaus, A., Klück, H.-C., Seiffert, U., Fischer, M., Voegele, R. T., Töpfer, R., 2020b. Evaluating the suitability of hyper- and multispectral imaging to detect foliar symptoms of the grapevine trunk disease Esca in vineyards. Plant Methods 16, 142. https://doi.org/10.1186/s13007-020-00685-3.

Bendel, N., Kicherer, A., Backhaus, A., Köckerling, J., Maixner, M., Bleser, E., Klück, H.-C., Seiffert, U., Voegele, R.T., Töpfer, R., 2020c. Detection of grapevine leafroll-associated virus 1 and 3 in white and red grapevine cultivars using hyperspectral imaging. Remote Sens. 12, 1693. https://doi.org/10.3390/rs12101693.

Bertsch, C., Ramírez-Suero, M., Magnin-Robert, M., Larignon, P., Chong, J., Abou-Mansour, E., Spagnolo, A., Clément, C., Fontaine, F., 2013. Grapevine trunk diseases: complex and still poorly understood. Plant Pathol. 62, 243–265. https://doi.org/10.1111/j.1365-3059.2012.02674.x.

Bock, C.H., Poole, G.H., Parker, P.E., Gottwald, T.R., 2010. Plant disease severity estimated visually, by digital photography and image analysis, and by hyperspectral imaging. CRC. Crit. Rev. Plant Sci. 29 (2), 59–107. https://doi.org/10.1080/07352681003617285.

Carter, G.A., 1991. Primary and secondary effects of water content on the spectral reflectance of leaves. Am. J. Bot. 78 (7), 916–924. https://doi.org/10.1002/j.1537-2197.1991.tb14495.x.

Chong, I.-G., Jun, C.-H., 2005. Performance of some variable selection methods when multicollinearity is present. Chemom. Intell. Lab. Syst. 78 (1-2), 103–112. https://doi.org/10.1016/j.chemolab.2004.12.011.

Di Gennaro, S.F., Battiston, E., Di Marco, S., Facini, O., Matese, A., Nocentini, M., Palliotti, A., Mugnai, L., 2016. Unmanned Aerial Vehicle (UAV)-based remote sensing to monitor grapevine leaf stripe disease within a vineyard affected by esca complex. Phytopathol. Mediterr. 55, 262–275. https://doi.org/10.14601/Phytopathol_Mediterr-18312.

Fischer, M., Peighami Ashnaei, S., 2019. Grapevine, esca complex, and environment: the disease triangle. Phytopathol. Mediterr. 58, 17–37. https://doi.org/10.14601/Phytopathol_Mediterr-25086.

Fontaine, F., Gramaje, D., Armengol, J., Smart, R., Nagy, Z.A., Borgo, M., Rego, C., Corio-Costet, M.-F., 2016a. Grapevine trunk diseases. A review. OIV Publications, Paris, France.

Fontaine, F., Pinto, C., Vallet, J., Clément, C., Gomes, A.C., Spagnolo, A., 2016b. The effects of grapevine trunk diseases (GTDs) on vine physiology. Eur. J. Plant Pathol. 144 (4), 707–721. https://doi.org/10.1007/s10658-015-0770-0.

Fourty, T.h., Baret, F., Jacquemoud, S., Schmuck, G., Verdebout, J., 1996. Leaf optical properties with explicit description of its biochemical composition: Direct and inverse problems. Remote Sens. Environ. 56 (2), 104–117. https://doi.org/10.1016/0034-4257(95)00234-0.

Gao, Z., Khot, L.R., Naidu, R.A., Zhang, Q., 2020. Early detection of grapevine leafroll disease in a red-berried wine grape cultivar using hyperspectral imaging. Comput. Electron. Agric. 179, 105807. https://doi.org/10.1016/j.compag.2020.105807.

Gausman, H.W., 1974. Leaf reflectance of near-infrared. Photogramm. Eng. Remote Sensing 40, 183–191.

Gramaje, D., Úrbez-Torres, J.R., Sosnowski, M.R., 2018. Managing grapevine trunk diseases with respect to etiology and epidemiology: current strategies and future prospects. Plant Dis. 102 (1), 12–39. https://doi.org/10.1094/PDIS-04-17-0512-FE.

Graniti, A., Surico, G., Mugnai, L., 2000. Esca of grapevine: a disease complex or a complex of diseases? Phytopathol. Mediterr. 39, 16–20.

Guerin-Dubrana, L., Fontaine, F., Mugnai, L., 2019. Grapevine trunk disease in European and Mediterranean vineyards: occurrence, distribution and associated disease-affecting cultural factors. Phytopathol. Mediterr. 58, 49–71. https://doi.org/0.14601/Phytopathol_Mediterr-25153.

Jolliffe, I.T., 1986. Principal Component Analysis. Springer, New York, NY. https://doi.org/10.1007/978-1-4757-1904-8.

Junges, A.H., Almança, M.A.K., Fajardo, T.V.M., Ducati, J.R., 2020. Leaf hyperspectral reflectance as a potential tool to detect diseases associated with vineyard decline. Trop. Plant Pathol. 45 (5), 522–533. https://doi.org/10.1007/s40858-020-00387-0.

Junges, A.H., Ducati, J.R., Scalvi Lampugnani, C., Almança, M.A.K., 2018. Detection of grapevine leaf stripe disease symptoms by hyperspectral sensor. Phytopathol. Mediterr. 57, 399–406. https://doi.org/10.14601/Phytopathol_Mediterr-22862.

Knauer, U., Matros, A., Petrovic, T., Zanker, T., Scott, E.S., Seiffert, U., 2017. Improved classification accuracy of powdery mildew infection levels of wine grapes by spatial-spectral analysis of hyperspectral images. Plant Methods 13, 47. https://doi.org/10.1186/s13007-017-0198-y.

Kokaly, R.F., Skidmore, A.K., 2015. Plant phenolics and absorption features in vegetation reflectance spectra near 1.66 μm. Int. J. Appl. Earth Obs. Geoinf. 43, 55–83. https://doi.org/10.1016/j.jag.2015.01.010.

Lecomte, P., Darrieutort, G., Liminana, J.-M., Comont, G., Muruamendiaraz, A., Legorburu, F.-J., Choueiri, E., Jreijiri, F., El Amil, R., Fermaud, M., 2012. New insights into Esca of grapevine: the development of foliar symptoms and their association with xylem discoloration. Plant Dis. 96 (7), 924–934. https://doi.org/10.1094/PDIS-09-11-0776-RE.

Lopez-Molina, C., Ayala-Martini, D., Lopez-Maestresalas, A., Bustince, H., 2017. Baddeley's Delta metric for local contrast computation in hyperspectral imagery. Prog. Artif. Intell. 6 (2), 121–132. https://doi.org/10.1007/s13748-017-0111-y.

Lowe, A., Harrison, N., French, A.P., 2017. Hyperspectral image analysis techniques for the detection and classification of the early onset of plant disease and stress. Plant Methods 13, 80. https://doi.org/10.1186/s13007-017-0233-z.

MacDonald, S.L., Staid, M., Staid, M., Cooper, M.L., 2016. Remote hyperspectral imaging of grapevine leafroll-associated virus 3 in cabernet sauvignon vineyards. Comput. Electron. Agric. 130, 109–117. https://doi.org/10.1016/j.compag.2016.10.003.

Mahlein, A.-K., 2016. Plant disease detection by imaging sensors – parallels and specific demands for precision agriculture and plant phenotyping. Plant Dis. 100 (2), 241–251. https://doi.org/10.1094/PDIS-03-15-0340-FE.

Mahlein, A.-K., Kuska, M.T., Behmann, J., Polder, G., Walter, A., 2018. Hyperspectral sensors and imaging technologies in phytopathology: state of the art. Annu. Rev. Phytopathol. 56 (1), 535–558. https://doi.org/10.1146/annurev-phyto-080417-050100.

Mahlein, A.-K., Oerke, E.-C., Steiner, U., Dehne, H.-W., 2012. Recent advances in sensing plant diseases for precision crop protection. Eur. J. Plant Pathol. 133 (1), 197–209. https://doi.org/10.1007/s10658-011-9878-z.

Martín, L., Fontaine, F., Castaño, F.J., Songy, A., Roda, R., Vallet, J., Ferrer-Gallego, R., 2019. Specific profile of Tempranillo grapevines related to Esca-leaf symptoms and climate conditions. Plant Physiol. Biochem. 135, 575–587. https://doi.org/10.1016/j.plaphy.2018.10.040.

Meier, U., 2001. Growth stages of mono-and dicotyledonous plant. BBCH Monograph, 2nd ed. Federal Biological Research Centre for Agriculture and Forestry, Berlin.

Mobaraki, N., Amigo, J.M., 2018. HYPER-Tools. A graphical user-friendly interface for hyperspectral image analysis. Chemom. Intell. Lab. Syst. 172, 174–187. https://doi.org/10.1016/j.chemolab.2017.11.003.

Mondello, V., Songy, A., Battiston, E., Pinto, C., Coppin, C., Trotel-Aziz, P., Clément, C., Mugnai, L., Fontaine, F., 2018. Grapevine trunk diseases: a review of fifteen years of trials for their control with chemicals and biocontrol agents. Plant Dis. 102 (7), 1189–1217. https://doi.org/10.1094/PDIS-08-17-1181-FE.

Mugnai, L., Graniti, A., Surico, G., 1999. Esca (black measles) and brown wood-streaking: two old and elusive diseases of grapevines. Plant Dis. 83 (5), 404–418. https://doi.org/10.1094/PDIS.1999.83.5.404.

Nicolaï, B.M., Beullens, K., Bobelyn, E., Peirs, A., Saeys, W., Theron, K.I., Lammertyn, J., 2007. Nondestructive measurement of fruit and vegetable quality by means of NIR spectroscopy: A review. Postharvest Biol. Technol. 46 (2), 99–118. https://doi.org/10.1016/j.postharvbio.2007.06.024.

Nørgaard, L., Saudland, A., Wagner, J., Nielsen, J.P., Munck, L., Engelsen, S.B., 2000. Interval partial least-squares regression (iPLS): A comparative chemometric study with an example from near-infrared spectroscopy. Appl. Spectrosc. 54 (3), 413–419. https://doi.org/10.1366/0003702001949500.

Oerke, E.-C., Herzog, K., Toepfer, R., 2016. Hyperspectral phenotyping of the reaction of grapevine genotypes to Plasmopara viticola. J. Exp. Bot. 67 (18), 5529–5543. https://doi.org/10.1093/jxb/erw318.

Ollinger, S.V., 2011. Sources of variability in canopy reflectance and the convergent properties of plants. New Phytol. 189 (2), 375–394. https://doi.org/10.1111/j.1469-8137.2010.03536.x.

Osborne, B.G., Fearn, T., Hindle, P.T., 1993. Practical NIR Spectroscopy with Applications in Food and Beverage Analysis, 2nd ed. Longman Scientific and Technical, Harlow, UK.

Otsu, N., 1979. A threshold selection method from gray-level histograms. IEEE Trans. Syst. Man. Cybern. 9 (1), 62–66. https://doi.org/10.1109/TSMC.1979.4310076.

Pérez-Roncal, C., López-Maestresalas, A., Lopez-Molina, C., Jarén, C., Urrestarazu, J., Santesteban, L.G., Arazuri, S., 2020. Hyperspectral imaging to assess the presence of powdery mildew (Erysiphe necator) in cv. Carignan Noir grapevine bunches. Agronomy 10, 88. https://doi.org/10.3390/agronomy10010088.

Rajalahti, T., Arneberg, R., Berven, F.S., Myhr, K.-M., Ulvik, R.J., Kvalheim, O.M., 2009. Biomarker discovery in mass spectral profiles by means of selectivity ratio plot. Chemom. Intell. Lab. Syst. 95 (1), 35–48. https://doi.org/10.1016/j.chemolab.2008.08.004.

Rançon, F., Bombrun, L., Keresztes, B., Germain, C., 2019. Comparison of SIFT encoded and deep learning features for the classification and detection of Esca disease in Bordeaux vineyards. Remote Sens. 11, 1. https://doi.org/10.3390/rs11010001.

Ren, X., Malik, J., 2003. Learning a classification model for segmentation. Proceedings of the Ninth IEEE International Conference on Computer Vision. IEEE 10–17. https://doi.org/10.1109/ICCV.2003.1238308.

Rinnan, Å., Berg, F.V.D., Engelsen, S.B., 2009. Review of the most common pre-processing techniques for near-infrared spectra. TrAC Trends Anal. Chem. 28 (10), 1201–1222. https://doi.org/10.1016/j.trac.2009.07.007.

Sankaran, S., Mishra, A., Ehsani, R., Davis, C., 2010. A review of advanced techniques for detecting plant diseases. Comput. Electron. Agric. 72 (1), 1–13. https://doi.org/10.1016/j.compag.2010.02.007.

Savary, S., Willocquet, L., Pethybridge, S.J., Esker, P., McRoberts, N., Nelson, A., 2019. The global burden of pathogens and pests on major food crops. Nat. Ecol. Evol. 3 (3), 430–439. https://doi.org/10.1038/s41559-018-0793-y.

Savitzky, A., Golay, M.J.E., 1964. Smoothing and differentiation of data by simplified least squares procedures. Anal. Chem. 36 (8), 1627–1639. https://doi.org/10.1021/ac60214a047.

Serrano, L., Peñuelas, J., Ustin, S.L., 2002. Remote sensing of nitrogen and lignin in Mediterranean vegetation from AVIRIS data: Decomposing biochemical from structural signals. Remote Sens. Environ. 81 (2-3), 355–364. https://doi.org/10.1016/S0034-4257(02)00011-1.

Surico, G., 2009. Towards a redefinition of the diseases within the esca complex of grapevine. Phytopathol. Mediterr. 48, 5–10.

West, J.S., Bravo, C., Oberti, R., Lemaire, D., Moshou, D., McCartney, H.A., 2003. The potential of optical canopy measurement for targeted control of field crop diseases. Annu. Rev. Phytopathol. 41, 593–614. https://doi.org/10.1146/annurev.phyto.41.121702.103726.

Zhang, J., Huang, Y., Pu, R., Gonzalez-Moreno, P., Yuan, L., Wu, K., Huang, W., 2019. Monitoring plant diseases and pests through remote sensing technology: A review. Comput. Electron. Agric. 165, 104943. https://doi.org/10.1016/j.compag.2019.104943.